Density Functional Theory Analysis of Surface Structures of Spinel $LiNi_{0.5}Mn_{1.5}O_4$ Cathode Materials

Jianjian Shi,[1] Zhiguo Wang,[1*] Y.Q. Fu[1, 2*]

1 *School of Physical Electronics, University of Electronic Science and Technology of China, Chengdu, 610054, P.R. China*

2 *Department of Physics and Electrical Engineering, Faculty of Engineering and Environment, University of Northumbria, Newcastle upon Tyne, NE1 8ST, UK*

*Corresponding author. E-mail: zgwang@uestc.edu.cn(ZW); richard.fu@northumbria.ac.uk(YF)

Abstract

First-principle calculation was employed to investigate the surface stability for (100), (110) and (111) low index facets of $LiNi_{0.5}Mn_{1.5}O_4$ (LNMO) crystallographic structures with a $P4_332$ space group and phase transitions at the surface regions of $Ni_{0.5}Mn_{1.5}O_4$. The calculated surface energies of (100) and (111) facets with Li-terminations are 1.39 and 1.40 eV, respectively, indicating that both these facets of the LNMO are stable according to the calculation results. Defect formation energies and diffusion barriers of Ni and Mn in surface facets of the $Ni_{0.5}Mn_{1.5}O_4$ are much lower than those in the bulk. This suggests that the Ni and Mn ions in the surface regions of the LNMO easily occupy the tetrahedral Li-positions during delithiation process, which supports the experimental results and explains the surface structure changes of the LNMO upon delithiation.

Key words: $LiNi_{0.5}Mn_{1.5}O_4$, Lithium ion batteries, Surface, Density functional theory

1. Introduction

A typical lithium-ion batteries (LIBs) consist of anode, cathode and electrolyte. To cope with the great demands for high performance, scientists are designing and developing new electrode materials for the LIB_S. Recently, the electrochemical performance of the anode materials has been significantly improved [1-4]. Whereas cathode electrode materials with a high energy capacity and good thermal stability are becoming the critical factor for the successful applications of the LIBs into portable electric devices and plug-in hybrid electric vehicles. Spinel structural $LiNi_{0.5}Mn_{1.5}O_4$ (LNMO) crystal used as the cathode material for the LIBs has received much interest owing to its higher specific energy capacity of 146.6 mAh/kg, higher rate performance, and higher operating voltage (above 4.7 V) than those of the currently used cathode materials of $LiCoO_2$ and $LiFePO_4$ [5-8].

LNMO has two different crystal structures with $P4_332$ and Fd-3m space groups, which are related to the arrangements of atoms in the cells. For the LNMO with the $P4_332$ structure, Mn and Ni atoms occupy 4b and 12d sites, respectively. Li atoms occupy 8c sites, and O atoms occupy the 8c and 24e sites [9]. For the LNMO with the Fd-3m space group, Li ions are located at 8c sites. Mn and Ni ions are randomly distributed in 16d sites, and O ions occupy the 32e sites (as shown in Fig 1). These two types of the LNMO were synthesized experimentally and used as cathode materials for the LIBs [10]. The transformation of the LNMO from Fd-3m to $P4_332$ during high temperature annealing was found to occur at about 700 ^oC [10].

Yoon et al. found that the capacity of the LNMO with Fd-3m space group deteriorated rapidly at 60^oC upon lithiation/delithiation cycles [11]. The deterioration of the capacity causes

problems for the commercial application of the LNMO in practice, especially at high temperatures. To improve the electrochemical properties of the LNMO, nano- and micron-sized LNMO was synthesized and nano- and micron-scaling effects of the LNMO were investigated as the cathode electrode materials for the LIBs [12-15]. Both experimental analysis and theoretical calculation indicated that the micron-sized LNMO can be used as a cathode material with a good rate performance [15].

Surface properties of the electrode materials play critical roles in the surface reactions and stability during electrochemical cycling for LIBs [16, 17]. Surface modifications of the LNMO spinel materials using carbons, AlF_3, nano-Y_2O_3, TiO_2 and Al_2O_3 coatings have been explored to improve their electrochemical performance [12, 18-20]. Results indicated that the surface properties of electrode materials have a prominent effect on electrochemical properties of the LNMO used as cathode materials for LIBs. Lee et al. [14, 21] have investigated the surface stability of LNMO using the density functional theory (DFT). They predicted that the (111) facet is the energetic favorable surface for the LNMO and concluded that nano-scale LNMO as the cathode electrode material can improve the electrochemical properties of the LIBs, such as rate capability. Hai et al. [22] experimentally found that the rate capability and diffusion properties of the LNMO single crystal with a (111) surface are superior to the one with a (112) surface.

The surface atomistic structures of electrode materials can be easily identified using transmission electron microscope (TEM) and scanning TEM (STEM) [23-25]. Several TEM/STEM studies have revealed Ni tends to segregate on the surface the LNMO cathode,

which results in a structural transition [24]. Recently, Pan et al. [26] investigated the surface facet segregation of Ni and Co in the LNMO using intensive aberration corrected STEM. They found that Ni and Co show strong facet selectivity when building up their surface segregation layers: Ni prefer to segregate on (200) crystalline plane of Li-Mn-rich oxide whereas Co has a strong preference to (20-2) one [26]. Lin et al. [27] found using an STEM that a layer of Mn_3O_4-like structure with a thickness of ~2 nm was observed on the surface of the LNMO cathode materials during the initial charging to 4.9 V. They found that the surface phase transition resulted in the diffusion of Ni/Mn ions into the Li ion positions. DFT simulations have been successfully used to show that the O deficiency will promote Ni/Mn ions diffusion from octahedral positions to tetrahedral Li ion positions in the bulk LNMO [9].

Fundamental understanding of the surface structure and surface phase transition is crucial to improve the electrochemical performance of cathode materials. In this work, the surface energies of (100), (110) and (111) low index facets of the LNMO were investigated using the DFT. The diffusion of Ni/Mn ions on the surface NMO were investigated and compared with the experimental results.

2. Computational methods

Surface energies of (100), (110) and (111) facets and surface defect chemistry were calculated using the SIESTA (Spanish Initiative for Electronic Simulations with Thousands of Atoms) code [28] based on DFT [29, 30]. The electron exchange-correlation functional was described using generalized gradient approximation (GGA) with the Perdew-Burke-Emzerhof

(PBE) function [31]. Norm-conserving pseudo-potentials [32] were used to describe the interactions between the core electrons and valence electrons.

Simply employing the GGA by the omission of on-site coulomb interaction is considered to be insufficient to capture the correct electronic state of materials. GGA+U can improve the description of the electronic structure. The surface properties of the spinel $LiMn_2O_4$ were studied by Karim et al. [33] using both the GGA and GGA+U for the electron exchange-correlation function. However simulation results demonstrated that although the surface energies calculated using the GGA and GGA+U differ by the absolute values, the resulting Wulff shapes obtained using these two are comparable due to their similar relative surface energies. We have also calculated the diffusion barriers in the bulk LNMO using GGA+U, and the results showed that the energy barrier is 3.6 eV for the Ni to diffuse from its original lattice site to an tetrahedral site [9]. As will be discussed in the Results Section, the diffusion barrier calculated is 3.7 eV for the Ni diffuse along the same path by the omission of the on-site coulomb interaction. Therefore, we conclude that the omission of the on-site coulomb interaction in our work would not significantly affect our conclusion.

The valence electron wave functions were expanded using double-ζ basis functions. An energy cutoff of 150 Ry was used for the Fourier expansion of the density and the Monkhorst Pack of *k* points (4×4×4 and 4×4×1 for bulk and surface calculations, respectively) was used for sampling the Brillouin zone. Atomic positions in the pristine crystal structure and the surface structure were relaxed until the forces on each atom became less than 0.02 eV/Å. A vacuum layer of 25 Å was used to avoid the interactions between adjacent surfaces.

The surface energies (ΔE_{surf}) were calculated using Equation (1) [34].

$$\Delta E_{surf} = \Delta E_{cl} + \Delta E_{rel} \quad (1)$$

where ΔE_{cl} is the cleavage energy, which is defined as the energy required per unit area to split the bulk crystalline structure into two complementary surfaces on either side of the vacuum slab. ΔE_{rel} represents the energy difference between the relaxed surface structure and unrelaxed one. ΔE_{cl} and ΔE_{rel} were calculated using Equations (2) and (3), respectively.

$$\Delta E_{cl}(T_1 + T_2) = \frac{1}{4A}\left[E^{unR}(T_1) + E^{unR}(T_2) - nE_{cell}\right] \quad (2)$$

where A is the area of T_1 - or T_2-terminated surfaces; $E^{unR}(T_1)$ and $E^{unR}(T_2)$ refer to the total energies of the unrelaxed structures with T_1 - and T_2 -terminated surfaces, respectively; E_{cell} is the total energy of the bulk cell, and n is the total number of bulk units in these two complementary surface structures. The value of 1/4 was used indicating that four surfaces are created upon the crystal cleavage.

The relaxation energies ΔE_{rel} for the T-terminated surface can be defined as

$$\Delta E_{rel}(T) = \frac{1}{2A}\left[E^{R}_{surf}(T) + E^{unR}_{surf}(T)\right] \quad (3)$$

where $E^{R}_{surf}(T)$ and $E^{unR}_{surf}(T)$ are the total energy of T-terminated surfaces which have been relaxed and unfixed, respectively. The value of 1/2 used means that two surfaces are created upon crystal cleavage.

The defect formation energy of the TM_{tetral}-Vac_{TM} complex was calculated using equation (4). This defect complex is composed of transition metal (Ni or Mn) moving to tetrahedral site with transition metal vacancy in its original lattice position:

$$\Delta E = E(\mathrm{TM}_{\mathrm{tetral}} - \mathrm{Vac}_{\mathrm{TM}}) - E(\mathrm{perf}) \quad (4)$$

where the $E(\mathrm{TM}_{\mathrm{tetral}} - \mathrm{Vac}_{\mathrm{TM}})$ and $E(\mathrm{perf})$ are the total energies of NMO bulk or slab with and without Ni- and Mn-V_{Tetra} TM_{tetral}-Vac_{TM} defect complex, respectively.

3. Results and discussions

The LNMO is composed of Li/Ni/Mn/O(1)-, Mn/O-, Li/Ni/Mn/O(2)-, Ni/Mn/O-atomic layers stacking in a sequence along the [110] direction as shown in Fig. 1. Therefore, the (110) surface of the LNMO can be terminated with Li/Ni/Mn/O(1)-, Mn/O-, Li/Ni/Mn/O(2)-, or Ni/Mn/O-atomic layers. Here we defined the two adjacent layers as complementary layers. Two pairs of complementary layers in [RF1] (110) plane, i.e. Ni/Mn/O- and Li/Ni/Mn/O(1)-terminated surfaces, Mn/O- and Li/Ni/Mn/O(2)-terminated surfaces, are shown in Fig. 1 as the part enclosed by dashed rectangles. The (110) surfaces with different terminations can be obtained by cutting the bonds between two complementary layers, as shown in Figs. 2a, 2b, 2c and 2d. All the possible terminations of (100), (110) and (111) surfaces of the LNMO are considered and given in Table 1.

The calculated surface energies of (100), (110) and (111) with different terminations are listed in Table 1. The (100) and (111) surfaces with Li-terminations have the lowest surface energies, which are 1.39 and 1.40 J/m^2, respectively. The (110) surfaces show large surface energies over 2.0 J/m^2. These results indicate that both the (100) and (111) facets are more energy stable surfaces. The atomic configurations of the (100) and (111) surfaces of the LNMO terminated with Li-layers are shown in Fig. 3 before and after relaxation. It can be seen from

this figure that the surface Li moves inward to the second layer with a displacement of about 0.45~0.90 Å for the (100) surface and 0.15~0.23 Å for the (111) surface, respectively. Other motions of surface atoms to the second layer are also observed but with a smaller displacement. For example, the Ni/Mn/O terminated layer moves to the sub-layer with a displacement of about 0.09~0.15 Å for the (100) surface, and the O- and Ni/Mn-terminated layers move to its sub-layer with displacements of 0.04~0.20 Å and 0.05-0.12 Å for the (111) surface, respectively. The atoms in the second layer and inside of the slabs do not show apparent atomic displacements.

STEM observation showed that the delithiated LNMO samples have different atomic configurations compared with the spinel structures at the surface upon initial delithiation [27]. It was found that the Ni or Mn ions move to the tetrahedral sites of the spinel structure at the surface, which was previously occupied by the Li ions before the delithiation process. The migration of the Ni/Mn ions from the octahedral sits to the tetrahedral sites has also been observed in the spinel LNMO upon heating [9, 27, 35, 36].

In order to understand the defect formation on the surface, the defect formation energies of TM_{tetral}-Vac_{TM} complex in the bulk and (110) surface of a fully delithiated LNMO (namely NMO) were calculated using equation (4) and the results are listed in Table 2. The defect formation energies of the Ni_{tetral}-Vac_{Ni} and Mn_{tetral}-Vac_{Mn} complex are 2.13 and 2.51 eV in the bulk NMO, respectively. These values are decreased to 1.25 and 1.31 eV when these complex appear on the (110) surface of the NMO, respectively. The defect formation energies are

significantly reduced compared with those in the bulk counterpart, which indicates that the TM_{tetral}-Vac_{TM} complex tends to form on the surface of the NMO.

The diffusion energy barriers for the Ni migration from the octahedral site to the tetrahedral site in (110) surface and bulk of NMO are shown in Fig. 4(a), i.e., migrating form crystalline lattice site to an interstitial site. The calculated diffusion barriers are 3.70 eV and 1.48 eV for the Ni diffusion in bulk and surface of the NMO, respectively. This indicates that it is easier for the Ni atom to diffuse from an octahedral site to the tetrahedral site on the surface of NMO than in the bulk during the delithiation process. The energy curves of the Ni diffusion on the surface are quite different compared with those in the bulk. A new metastable position appears when the Ni diffuses from the octahedral site to the tetrahedral site on the (110) surface. Several key positions along the migration path in the bulk and on the surfaces are shown in Figs. 4 (b) and (c), respectively. The Ni diffuses from the octahedral site to a neighboring tetrahedral site by passing through a tetrahedral site enclosed by four oxygen atoms with an energy barrier of 3.70 eV as shown in Fig. 4 (b). Whereas the Ni diffuses on the (110) surface from the octahedral site to a metastable B site by passing through a polydral composed of seven oxygen atoms with a Ni-O bond length of 1.33~2.97 Å. Ni is surrounded by six oxygen atoms with the Ni-O bond length of 1.99~2.33 Å as it occupies an octahedral interstitial (B) site, as shown in Fig. 4(c). Ni also diffuses from the metastable octahedral interstitial site to the surface tetrahedral site by passing through another octahedral composed of six oxygen atoms (with a Ni-O bonding length of 1.73~2.57 Å) with an energy barrier of 0.75 eV. The results should be related to the surface reconstruction of the NMO.

The surface atomic layer of the transitional metal moves to its sublayer by a displacement of about 0.18~0.19 Å on the (110) surface the NMO. Accordingly, the surface spinel structure is destroyed, but the result does not show much change of the bond for both the sublayer and the bulk. This causes that the surface tetrahedral Li-positions are different from the bulk with atomistic configurations. On the surface, the diffusion paths of the Ni from the octahedral site to the tetrahedral site will be blocked once the Ni atoms occupy the octahedral interstitial site. According to diffusion energy barrier curves of the Ni on (110) surface of the NMO (see Fig. 4a), the diffusion energy barrier is 1.44 eV when the Ni migrates from the Ni octahedral site to the octahedral interstitial site. Whereas the energy barrier is 0.75 eV when the Ni migrates from the octahedral site to a nearest tetrahedral one.

The diffusion of Mn in the bulk and surface layer of the NMO show similar behaviors as those of the Ni as shown in Fig. 5. The diffusion barriers are 3.39 and 1.80 eV for bulk and surface diffusions, respectively. Two metastable sites of B and C (as shown in Fig. 5) also appear when the Mn diffuses in the surface of the NMO.

The above results clearly indicate that the Ni/Mn atoms in the octahedral site will migrate to the tetrahedral site on the surface of the LNMO when the octahedral interstitial sites are occupied by the Ni/Mn. Results suggest that the transitional metal atoms diffuse easily from the octahedral site to the tetrahedral Li-positions on the surface of the LNMO crystallographic structure during the delithiation process, which agrees well with the previous experimental observation [27].

4. Conclusions

Surface structures of the LNMO and defect chemistry on the (110) surface of a fully-delithiated LNMO were studied using the DFT. The calculated results indicate that the (100) and (111) surfaces of the LNMO are energy stable than that of (110) surface. Defect formation energies and diffusion barriers of Ni and Mn are much lower in the (110) surface than those in the bulk material. TM_{tetral}-Vac_{TM} complex could be easily formed on (110) surfaces, which strongly supports the previous experimental observation [27].

Acknowledgement:

This work was financially supported by the National Natural Science Foundation of China (11474047). Funding support from Royal academy of Engineering UK-Research Exchange with China and India is acknowledged.

Compliance with Ethical Standards:

Funding: This study was funded by National Natural Science Foundation of China (11474047) and Royal academy of Engineering UK-Research Exchange with China and India.

Conflict of Interest: The authors declare that they have no conflict of interest.

References:

[1] Jianjian Shi WS, Wei Jin, Guangqiang Yin (2015) Diffusion of Lithium in α-Sn and β-Sn as Anode Materials for Lithium Ion Batteries, International Journal of ELECTROCHEMICAL Science and Technology of Advanced Materials 10: 4793 - 4800.

[2] Zhang PP, Ma ZS, Wang Y, et al. (2015) A first principles study of the mechanical properties of Li-Sn alloys, Rsc Adv 5: 36022-36029.

[3] Zhu XY, Yang DJ, Li JJ, Su FB (2015) Nanostructured Si-Based Anodes for Lithium-Ion Batteries, J Nanosci Nanotechno 15: 15-30.
[4] Zhang F, Yang X, Xie YQ, Yi NB, Huang Y, Chen YS (2015) Pyrolytic carbon-coated Si nanoparticles on elastic graphene framework as anode materials for high-performance lithium-ion batteries, Carbon 82: 161-167.
[5] Ozawa K (1994) Lithium-ion rechargeable batteries with LiCoO2 and carbon electrodes: the LiCoO2/C system, Solid State Ionics 69: 212-221.
[6] Hudaya C, Park JH, Lee JK, Choi W (2014) SnO2-coated LiCoO2 cathode material for high-voltage applications in lithium-ion batteries, Solid State Ionics 256: 89-92.
[7] Goodenough JB (2007) Cathode materials: A personal perspective, Journal of Power Sources 174: 996-1000.
[8] Yang S, Song Y, Ngala K, Zavalij PY, Stanley Whittingham M (2003) Performance of LiFePO4 as lithium battery cathode and comparison with manganese and vanadium oxides, Journal of Power Sources 119-121: 239-246.
[9] Wang Z, Su Q, Deng H, Fu Y (2015) Oxygen Deficiency and Defect Chemistry in Delithiated Spinel LiNi0.5Mn1.5O4Cathodes for Li-Ion Batteries, Chemelectrochem 2: 1182-1186.
[10] Park SH, Oh SW, Kang SH, Belharouak I, Amine K, Sun YK (2007) Comparative study of different crystallographic structure of LiNi0.5Mn1.5O4−δ cathodes with wide operation voltage (2.0–5.0V), Electrochimica Acta 52: 7226-7230.
[11] Yoon T, Park S, Mun J, et al. (2012) Failure mechanisms of LiNi0.5Mn1.5O4 electrode at elevated temperature, Journal of Power Sources 215: 312-316.
[12] Cho HM, Chen MV, MacRae AC, Meng YS (2015) Effect of Surface Modification on Nano-Structured LiNi0.5Mn1.5O4 Spinel Materials, ACS applied materials & interfaces 7: 16231-16239.
[13] Tang X, Jan SS, Qian Y, et al. (2015) Graphene wrapped ordered LiNi0.5Mn1.5O4 nanorods as promising cathode material for lithium-ion batteries, Sci Rep 5: 11958.
[14] Lee E, Persson KA (2014) Corrigendum: First-principles study of the nano-scaling effect on the electrochemical behavior in LiNi0.5Mn1.5O4(2013Nanotechnology24 424007), Nanotechnology 25: 159501.
[15] Ma X, Kang B, Ceder G (2010) High Rate Micron-Sized Ordered LiNi[sub 0.5]Mn[sub 1.5]O[sub 4], Journal of The Electrochemical Society 157: A925.
[16] Daheron L, Martinez H, Dedryvere R, et al. (2009) Surface Properties of LiCoO2 Investigated by XPS Analyses and Theoretical Calculations, J Phys Chem C 113: 5843-5852.
[17] Lin HB, Zhang YM, Rong HB, et al. (2014) Crystallographic facet- and size-controllable synthesis of spinel LiNi0.5Mn1.5O4with excellent cyclic stability as cathode of high voltage lithium ion battery, J Mater Chem A 2: 11987.
[18] Wang H, Shi Z, Li J, et al. (2015) Direct carbon coating at high temperature on LiNi0.5Mn1.5O4 cathode: Unexpected influence on crystal structure and electrochemical performances, Journal of Power Sources 288: 206-213.
[19] Wu Q, Yin Y, Sun S, Zhang X, Wan N, Bai Y (2015) Novel AlF3 surface modified spinel LiMn1.5Ni0.5O4 for lithium-ion batteries: performance characterization and mechanism exploration, Electrochimica Acta 158: 73-80.

[20] Wen WC, Yang XK, Wang XY, Shu LGH (2015) Improved electrochemical performance of the spherical LiNi0.5Mn1.5O4 particles modified by nano-Y2O3 coating, Journal of Solid State Electrochemistry 19: 1235-1246.
[21] Eunseok L, Kristin AP (2013) First-principles study of the nano-scaling effect on the electrochemical behavior in LiNi 0.5 Mn 1.5 O 4, Nanotechnology 24: 424007.
[22] Hai B, Shukla AK, Duncan H, Chen G (2013) The effect of particle surface facets on the kinetic properties of LiMn1.5Ni0.5O4cathode materials, J. Mater. Chem. A 1: 759-769.
[23] Zheng J, Xu P, Gu M, et al. (2015) Structural and Chemical Evolution of Li- and Mn-Rich Layered Cathode Material, Chemistry of Materials 27: 1381-1390.
[24] Gu M, Belharouak I, Genc A, et al. (2012) Conflicting Roles of Nickel in Controlling Cathode Performance in Lithium Ion Batteries, Nano Lett. 12: 5186-5191.
[25] Boulineau A, Simonin L, Colin J-F, Bourbon C, Patoux S (2013) First Evidence of Manganese–Nickel Segregation and Densification upon Cycling in Li-Rich Layered Oxides for Lithium Batteries, Nano Lett. 13: 3857-3863.
[26] Yan P, Zheng J, Zheng J, et al. (2016) Cathode Materials: Ni and Co Segregations on Selective Surface Facets and Rational Design of Layered Lithium Transition-Metal Oxide Cathodes (Adv. Energy Mater. 9/2016), Advanced Energy Materials 6: n/a-n/a.
[27] Lin M, Ben L, Sun Y, et al. (2015) Insight into the Atomic Structure of High-Voltage Spinel LiNi0.5Mn1.5O4Cathode Material in the First Cycle, Chemistry of Materials 27: 292-303.
[28] Soler JM, Artacho E, Gale JD, et al. (2002) The SIESTA method for ab initio order-N materials simulation, J Phys-Condens Mat 14: 2745-2779.
[29] Legrain F, Malyi O, Manzhos S (2015) Insertion energetics of lithium, sodium, and magnesium in crystalline and amorphous titanium dioxide: A comparative first-principles study, Journal of Power Sources 278: 197-202.
[30] Legrain F, Malyi OI, Manzhos S (2014) Comparative computational study of the energetics of Li, Na, and Mg storage in amorphous and crystalline silicon, Computational Materials Science 94: 214-217.
[31] Kim S, Aykol M, Wolverton C (2015) Surface phase diagram and stability of (001) and (111)LiMn2O4spinel oxides, Phys Rev B 92.
[32] Troullier N, Martins JL (1991) EFFICIENT PSEUDOPOTENTIALS FOR PLANE-WAVE CALCULATIONS, Physical Review B 43: 1993-2006.
[33] Karim A, Fosse S, Persson KA (2013) Surface structure and equilibrium particle shape of the LiMn2O4spinel from first-principles calculations, Phys Rev B 87.
[34] Cui J, Liu W (2010) First-principles study of the (001) surface of cubic BiAlO3, Physica B: Condensed Matter 405: 4687-4690.
[35] Hu EY, Bak SM, Liu J, et al. (2014) Oxygen-Release-Related Thermal Stability and Decomposition Pathways of LixNi0.5Mn1.5O4 Cathode Materials, Chemistry of Materials 26: 1108-1118.
[36] Nam KW, Bak SM, Hu EY, et al. (2013) Combining In Situ Synchrotron X-Ray Diffraction and Absorption Techniques with Transmission Electron Microscopy to Study the Origin of Thermal Instability in Overcharged Cathode Materials for Lithium-Ion Batteries, Adv Funct Mater 23: 1047-1063.

Table 1 Surface energies (ΔE_{surf}) of the (100), (110) and (111) facets for $LiNi_{0.5}Mn_{1.5}O_4$ crystalline structure.

	Termination	$\Delta E_{surf}(J/m^2)$
(100)	Li	1.39
	Ni/Mn/O	1.56
(110)	Li/Ni/Mn/O(1)	2.04
	Ni/Mn/O	2.11
	Mn/O	2.15
	Li/Ni/Mn/O(2)	2.12
(111)	Ni/Mn(1)	5.09
	O(1)	4.93
	O(2)	2.54
	Li(1)	2.41
	Ni/Mn(2)	1.66
	Li(2)	1.40

Table 2 Defect formation energies of Ni and Mn-V_{Tetra} in $Ni_{0.5}Mn_{1.5}O_4$ with space group $P4_332$ surface structure with (110) facets and the bulk crystallographic structure.

Atom	Formation energy (eV)	
	Surface	Bulk
Ni	1.25	2.13
Mn	1.32	2.51

Figure captions:

Figure 1. Crystalline structure of (110) plane of LNMO. There are two complementary surfaces for the (110) plane as labeled in two rectangular dashed lines, in which Ni/Mn/O- and Li/Ni/Mn/O-terminated surfaces, Mn/O- and Li/Ni/Mn/O-terminated surfaces are mutually complementary ones, respectively.

Figure 2. (a) and (b) surface crystalline structures are complementary surfaces with Ni/Mn/O - and Li/Ni/Mn/O (1)-terminated surfaces, (c) and (d) are complementary surfaces with Mn/O- and Li/Ni/Mn/O (2)-terminated surfaces.

Figure 3. (a) Unrelaxed and (b) relaxed (100) surface structures of with Li-terminations; (c) unrelaxed and (d) relaxed (111) surface structures with Li-terminations.

Figure 4. (a) The diffusion energy curve of Ni in surface and bulk NMOs, in which the red and black lines refer to surface and bulk energy curves, respectively. (b) Bulk and (c) (110) surface of NMO crystalline structures, in which blue balls refer to the migrating Ni atoms in different states. I and F refer to the initial and final states of Ni, respectively. A, B and C are the metastable states.

Figure 5. (a) Diffusion energy curves of Mn in surface and bulk NMOs, in which the red and black lines refer to surface and bulk energy curves, respectively. (b) Bulk and (c) (110) surface of NMO crystalline structures, in which black balls refer to the migrating Mn atoms in different states. I and F refer to the initial and final states of Ni, respectively. A, B, C and D are the metastable states.

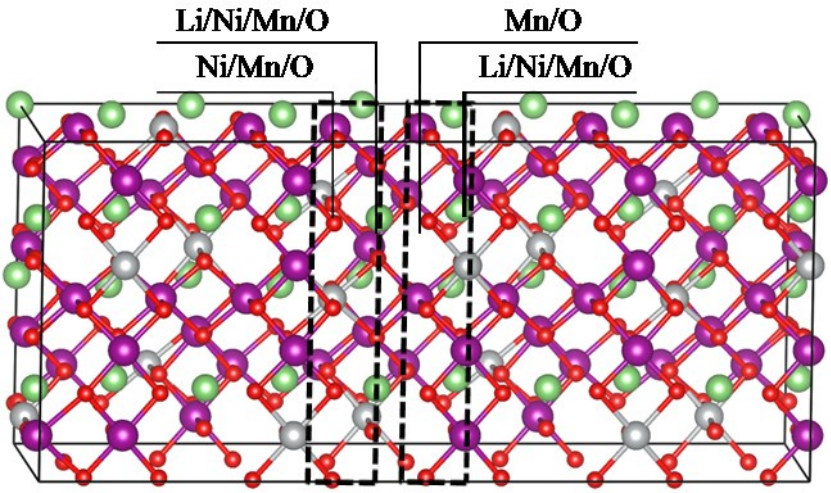

J.J. Shi et al. Figure 1

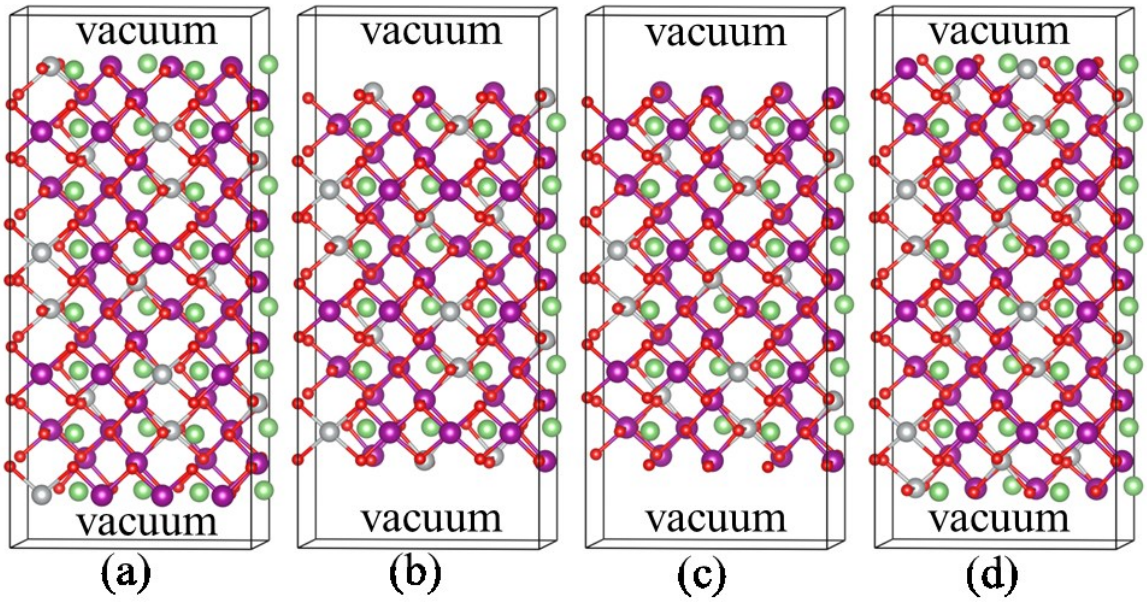

J.J. Shi et al. Figure 2

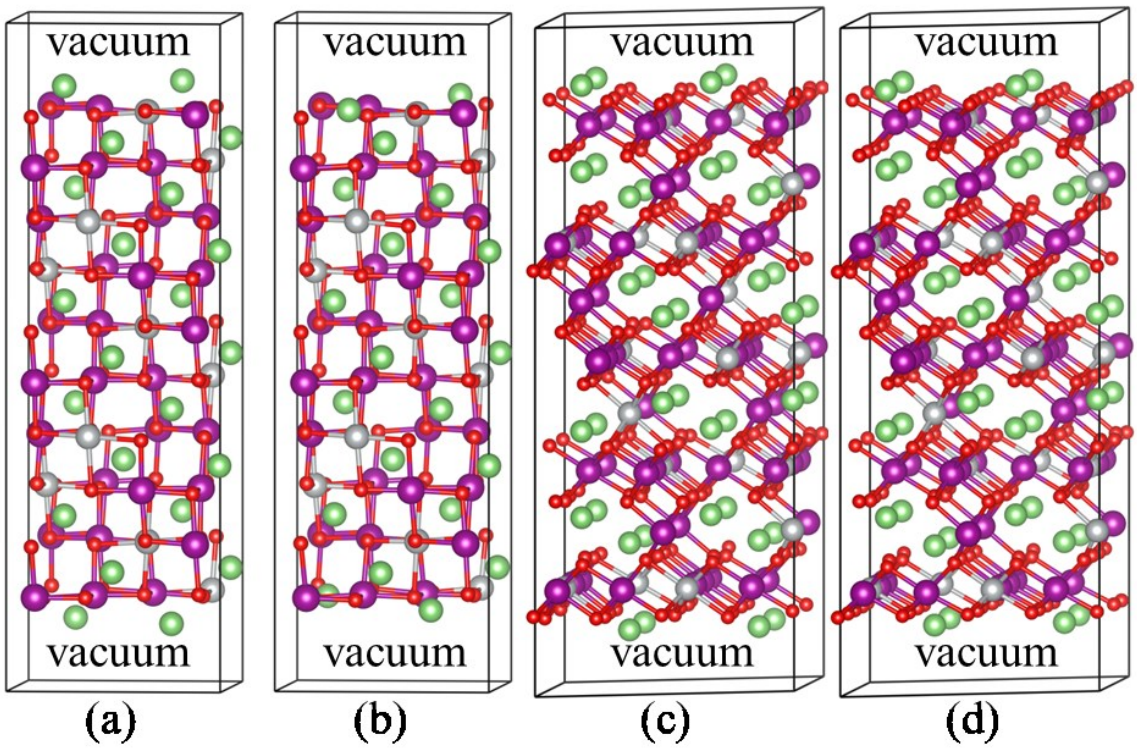

J.J. Shi et al. Figure 3

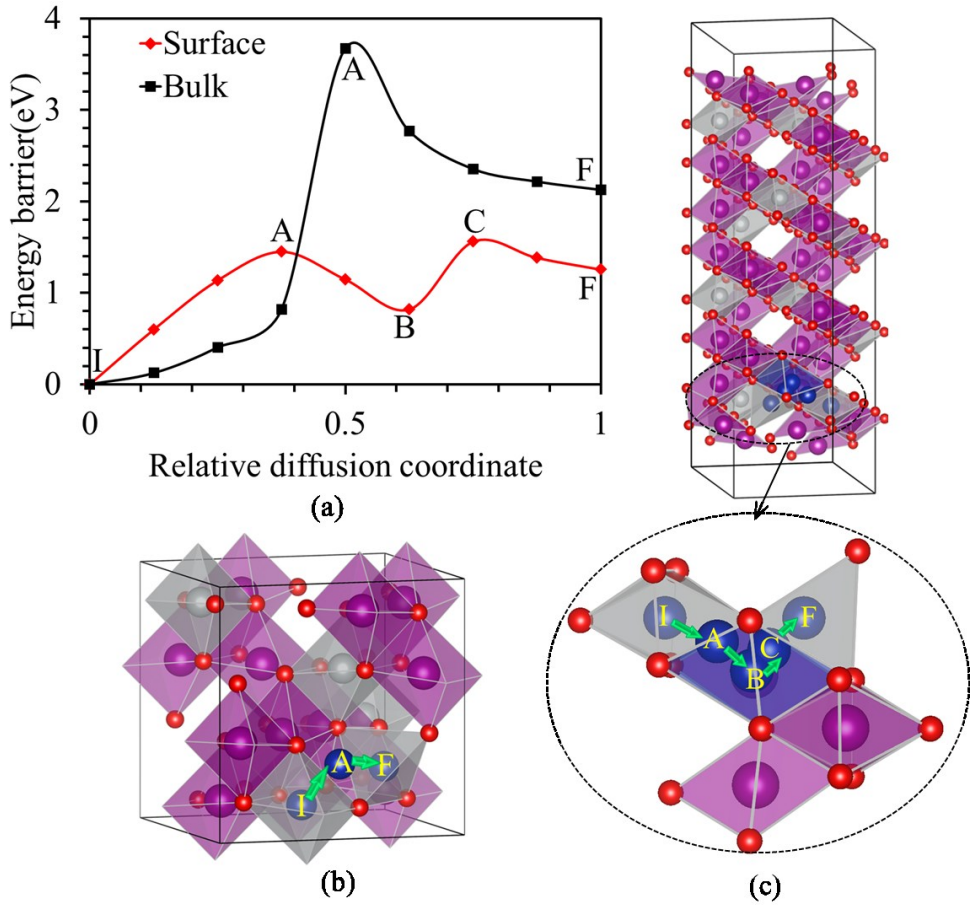

J.J. Shi et al. Figure 4

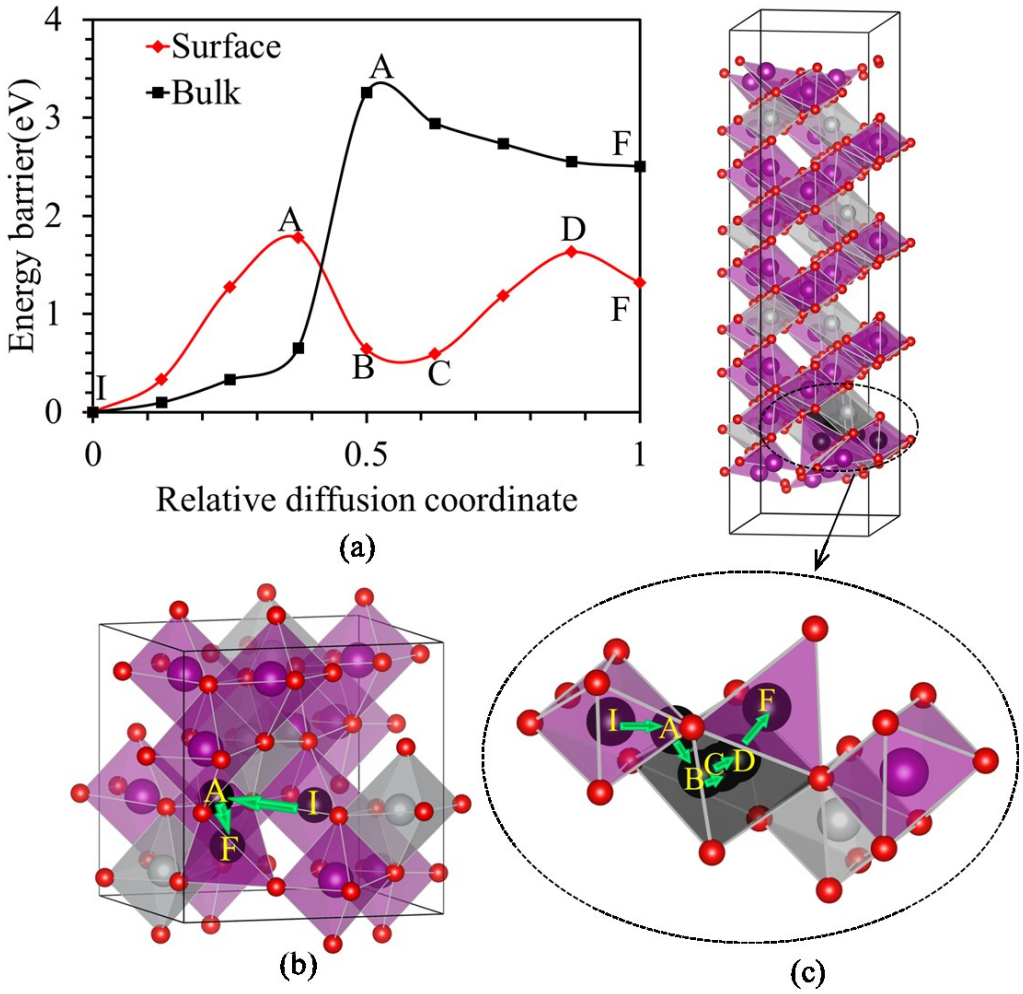

J.J. Shi et al. Figure 5